

MICROCOPY

CHART

①

Influence of  $Al_2O_3$  on Properties of  
Yttria Stabilized Zirconia- $Al_2O_3$  Composites

by

R. C. Buchanan and W. W. Davison

AD-A167 328

DTIC  
ELECTE  
MAY 06 1986  
S D  
D



**DISTRIBUTION STATEMENT A**  
Approved for public release;  
Distribution Unlimited

DTIC FILE COPY

DEPARTMENT OF CERAMIC ENGINEERING  
UNIVERSITY OF ILLINOIS  
URBANA, ILLINOIS

①

Final Report  
Technical Report No. 13  
Contract No.: US NAVY-N-00014-80-K-0969

Influence of  $Al_2O_3$  on Properties of  
Yttria Stabilized Zirconia- $Al_2O_3$  Composites

by

R. C. Buchanan and W. W. Davison

March, 1986

Department of Ceramic Engineering  
University of Illinois at Urbana-Champaign  
105 S. Goodwin Avenue  
Urbana, IL 61801

Research was supported by the Office of Naval Research  
Metallurgy and Ceramics Program  
Department of the Navy

Production in whole or in part is permitted for any purpose  
of the United States Government

This document has been approved  
for public release and sale; its  
distribution is unlimited.

DTIC  
ELECTE  
MAY 06 1986  
S D D



ABSTRACT

SECURITY CLASSIFICATION OF THIS PAGE

Composite structures of yttria (4.5 mol%) stabilized zirconia (YSZ) with added  $Al_2O_3$  (0.3 to 7.5 wt%) were investigated. Pressed YSZ compacts prepared from submicrometer powders of >99% purity were sintered in the range 1200-1350°C for 0.5 to 24 h. Uniform grain size microstructures (0.2 to 0.4  $\mu m$ ) were obtained which showed discrete  $Al_2O_3$  grains dispersed throughout. X-ray diffraction and Raman spectral analysis indicated a combination of both cubic and tetragonal phases. Measured lattice parameters were observed to vary irregularly with  $Al_2O_3$  content. DC conductivity was found to increase with added  $Al_2O_3$  less than 3 wt%. Strength values obtained for the composites were in excess of  $9 \text{ MPa} \cdot \text{m}^{1/2}$  ( $K_{Ic}$ ) and 425 MPa (MOR), significantly higher than reported for cubic phase YSZ. The increased strength was attributed to small grain size as well as to crack deflection and arrest mechanisms associated with the dispersed high modulus and lower expansion second phase. The presence of a monoclinic phase was not detected in the samples either before or after fracture, hence the strengthening could not be ascribed to transformation toughening.

Microstructure  $9 \text{ MPa} \cdot \text{m}^{1/2}$  X the Square root of M

$K_{Ic}$

Transformation toughening

SECURITY CLASSIFICATION OF THIS PAGE

TABLE OF CONTENTS

	PAGE
I. Introduction.....	3
II. Experimental.....	5
III. Results and Discussion.....	7
IV. Conclusions.....	14
V. Acknowledgments.....	15
VI. References.....	16
IV. List of Figures.....	24

RE: Distribution Statement  
 Approved for Public Release.  
 Per Dr. Paul Smith, ONR/Code 1131

Accession For	
NTIS CRA&I	<input checked="" type="checkbox"/>
DTIC TAB	<input type="checkbox"/>
Unannounced	<input type="checkbox"/>
Justification .....	
By .....	
Distribution /	
Availability Codes	
Dist	Avail and/or Special
A-1	



## Influence of $\text{Al}_2\text{O}_3$ on Properties of Yttria Stabilized Zirconia- $\text{Al}_2\text{O}_3$ Composites

### 1. Introduction

The use of improved processing techniques<sup>1,2</sup> and ultrafine powders have reduced sintering temperatures for zirconia from  $>1700^\circ\text{C}$  to  $<1400^\circ\text{C}$ .<sup>3-6</sup> Microstructures resulting from this lower temperature sintering show smaller and more uniform grain sizes, with resultant higher strengths and fracture toughness.<sup>7,8</sup>

Additives such as  $\text{MgO}$ ,  $\text{SiO}_2$ ,  $\text{Fe}_2\text{O}_3$ ,  $\text{B}_2\text{O}_3$ ,  $\text{TiO}_2$  and  $\text{Bi}_2\text{O}_3$  have been investigated as sintering aids for zirconia.<sup>9,10</sup> Various theories as to the mechanism by which these intentionally added impurities enhance the densification have been advanced.<sup>11,12</sup> Most involve a segregation of the impurities to the grain boundaries, where a comparatively low melting eutectic may be formed, resulting in liquid phase assisted sintering.<sup>10</sup> Another non-conflicting analysis contends that a major effect of the grain boundary impurities is to increase the pore drag force, minimizing pore-grain boundary breakaway and entrapped porosity.<sup>10,13</sup>

Use of  $\text{Al}_2\text{O}_3$  as an additive to the yttria-stabilized zirconia (YSZ) system has been investigated by many authors<sup>4-6,14,15</sup> and found to be an effective sintering aid. Bernard's<sup>6</sup> analysis of the mechanism of  $\text{Al}_2\text{O}_3$  assisted densification of YSZ held that  $\text{Al}^{3+}$  substituted for  $\text{Zr}^{4+}$  in the YSZ lattice (to  $\approx 0.1$  mol%) thus enhancing the sintering rate by accelerated cation diffusion. Butler and Drennan<sup>14</sup> proposed that the presence of  $\text{Al}_2\text{O}_3$  particles in a YSZ microstructure would scavenge the grain boundaries of  $\text{SiO}_2$  impurities, enabling faster grain boundary movement and therefore enhanced densification. Buchanan and Wilson<sup>5</sup> noted the presence of an intergranular liquid phase with  $\text{Al}_2\text{O}_3$  added to YSZ and a nonlinear relationship between

density and sintering time at different temperatures, indicative of particle rearrangement in the presence of an intergranular liquid phase. Buchanan and Wilson also noted excessively large  $\text{Al}_2\text{O}_3$  particles (with respect to the YSZ grain size), often with significant adjacent porosity.

The well documented strength enhancement of  $\text{ZrO}_2$  ceramics by a transformation toughening process is considered to be due to the mechanisms of<sup>16</sup>: 1) energy absorption near an advancing crack tip resulting from a martensitic (tetragonal  $\rightarrow$  monoclinic) phase transformation,<sup>17,18</sup> and 2) nucleation of matrix cracks and residual stresses due to particles which are transformed upon cooling before the specimen is loaded.<sup>19</sup> This toughening process has been found to take place, by Tsukuma et al., in 2 - 3.85 mol% YSZ with up to 40 wt%  $\text{Al}_2\text{O}_3$  added.<sup>20</sup> The authors attributed an observed increase in strength and fracture toughness with added  $\text{Al}_2\text{O}_3$  content to suppression of crack initiation within the YSZ.

Matsui et al.<sup>21</sup> have addressed the phenomenon whereby the tetragonal  $\rightarrow$  monoclinic transformation is hindered by a small grain size microstructure (grains  $< 0.5 \mu\text{m}$ ). This phenomenon has been speculated to occur as a result of 1) progression of the transformation being interrupted by grain boundaries; and 2) difficulty in nucleation of the monoclinic phase due to the small grain size. A shear deformation often accompanies the transformation due to the cooperative movement of ions, hence a critical grain size is required for the transformation to take place. Another effect, which has been noted by Rao,<sup>22</sup> is that  $\alpha\text{-Al}_2\text{O}_3$  particles can plastically deform in response to matrix strains in the partially stabilized  $\text{ZrO}_2$  lattice.

In this study the effect of increasing amounts of submicrometer  $\text{Al}_2\text{O}_3$  additions on the structure, rupture modulus, fracture toughness, and dc conductivity of a 4.5 mol% YSZ was investigated. The size and distribution

of the  $\text{Al}_2\text{O}_3$  phase regions and other microstructural features of the composite structure as a function of added  $\text{Al}_2\text{O}_3$  were also studied.

## II. Experimental

The starting powder used in this study was an 8.0 wt% (4.5 mol%) yttria-stabilized zirconia (YSZ), typical lot analysis and average particle size distribution for which is given in Table 1. X-ray diffraction analysis of the powder revealed only the cubic phase. The primary additive to the YSZ was a  $0.03 \mu\text{m}$   $\text{Al}_2\text{O}_3$  floated powder, but other  $\text{Al}_2\text{O}_3$  precursors including oxalate [ $\text{Al}_2(\text{C}_2\text{O}_4)_3$ ], hydroxide powder or gel [ $\text{Al}(\text{OH})_3$ ], were initially investigated, as shown in Table 2. After Scott et al.<sup>2</sup> residual chlorine present in the YSZ powder was reduced in concentration from 1.0% to  $\approx 0.05\%$  by washing with distilled water.

Fifty gram batches were prepared by adding 0-7.5 wt%  $\text{Al}_2\text{O}_3$  to the washed YSZ and ball milling for 12 h. Polypropylene jars and zirconia balls were used to minimize contamination, and a dispersing agent [2 ml Menahden (Z-3) fish oil] was added to each batch along with 200 ml of a 60:40 volume solution consisting of isopropanol and distilled water. A binder mixture consisting of 3 wt% PVA and 3 wt% carbowax 4000 was then added and milled for an additional 1.5 h immediately precedent to spray drying of the suspension. Pellets 1.6 cm in diameter and approximately 1.2 mm thick, and 3.1 x 0.4 x 0.4 cm bars were cold pressed at 220 MPa and 280 MPa respectively. The samples were fired in a  $\text{MoSi}_2$  resistance furnace on  $\text{ZrO}_2$  setters in air ambient. Sintering was carried out in the range 1200-1350°C for 0.5-24 h.

Sintered densities were measured by water displacement and He pycnometer techniques and theoretical densities were calculated using the cell dimensions determined from X-ray powder diffraction of the fired samples. The theoretical densities of samples containing  $\text{Al}_2\text{O}_3$  additions are given in

Table 3. These were calculated using a series mixing formula since the solubility of  $\text{Al}_2\text{O}_3$  in YSZ is quite low.<sup>5,6</sup>

Samples prepared for modulus of rupture tests (bars 2.5 x 0.4 x 0.2 cm) were polished on the side of tensile stress during breaking. Polishing was carried out with 45,30,15,6,1 and 0.25  $\mu\text{m}$  diamond paste after initial grinding on a 70  $\mu\text{m}$  diamond wheel. The lengthwise edges along the polished side were beveled at 45° and the resulting faces ( $\approx 0.5$  mm) were also polished. Strength values were determined with an Instron model 1125 strength tester equipped with a jig for four-point loading. Inner and outer spans on the jig were 2.3 and 1.2 cm, respectively, and a strain rate of 0.1 mm/min was used. Fracture toughness ( $K_{IC}$ ) measurements were made with a Tukon microhardness tester using the Vickers and Knoop indenters at loads (P) of 2.0, 2.5 and 3.0 kg to obtain values for the crack size,  $C_o$  and modulus of elasticity to hardness ratio (E/H), respectively. This loading range is considered adequate for the crack sizes measured according to Nihara et al.<sup>234</sup> The fracture toughness calculations were made from the formula:<sup>245</sup>

$$K_{IC} = 0.016 (E/H)^{1/2} P/C_o^{3/2} \quad (1)$$

A (Dupont 1090) Thermal Analyzer System was used to measure the thermal expansion of the samples. DC resistivity measurements were made with a (Beckman L-8) Megohmmeter up to  $\approx 300^\circ\text{C}$ ; above  $300^\circ\text{C}$ , measurements were continued using a (Hewlett Packard 4276A) LCZ Meter at 100 Hz to minimize ionic polarization effects. Coupling of the data from the two temperature regimes resulted in a linear curve. Samples were electroded with Pt paste fired at  $1100^\circ\text{C}$  prior to measurement.

Microstructures of the polished and thermally etched samples were analyzed using SEM (JEOL 35C) (ISI US130), STEM (Vacuum Generators HB5), TEM (Phillips 400T E.M.) and EDS (Kevex)(EDAX) microanalysis techniques. X-ray diffraction analyses were carried out on fired samples ground to -100 mesh

(also on fired pellets, fracture and polished surfaces) using a (Philips 3100) X-ray Generator with a (APD 3520) Diffractometer Control System. Scan speeds of 0.5 - 2.0° 2 $\theta$ /min were used. Grain size measurements were made from SEM photomicrographs of thermally etched and polished samples, using the Mendelsohn line intercept method.<sup>256</sup> TEM samples were prepared by grinding and polishing a 3 mm diameter sample to  $\approx$ 70  $\mu$ m thickness, followed by dimple grinding the center to  $\approx$ 15  $\mu$ m and finally by Ar ion milling.

Raman spectra were performed in a pseudo-backscattering arrangement with  $\approx$ 2  $\text{cm}^{-1}$  resolution using a homemade 1 m double monochromator with 200 mm slits. Laser excitation was provided by the 514.5 nm line of an argon-ion laser (Spectra-Physics).

### III. Results and Discussion

Property data obtained on the sintered YSZ samples containing the different size (0.3-10 $\mu$ m) Al<sub>2</sub>O<sub>3</sub> powders (0.325 wt%) all showed an increase in density (2.0 to 5.0%), MOR (10 to 50%) and K<sub>1C</sub> (25 to 50%) compared to the base YSZ sample. The magnitude of the increase was found to be inversely proportional to the particle size of the Al<sub>2</sub>O<sub>3</sub> precursor. Hence, in terms of optimum densification and properties, the 0.03  $\mu$ m floated Al<sub>2</sub>O<sub>3</sub> powder was determined to be the most effective additive to the YSZ, a result to be expected in view of the similarity in particle size. SEM photomicrographs in Figure 1 show morphologies and particle sizes of the YSZ and 0.03  $\mu$ m floated Al<sub>2</sub>O<sub>3</sub> powders (the main alumina additive used).

Figure 2 shows densification behavior for the YSZ + Al<sub>2</sub>O<sub>3</sub> (0.325 wt%) samples as a function of sintering temperature and soak time. The minimum time for achieving >99% ThD was found to be 1.5 hours at 1350°C. but, although fully dense, these samples showed evidence of discontinuous grain growth. Examination of the sintered microstructures to determine the

sintering time and temperature necessary to achieve full densification with minimal discontinuous grain growth found 8 h at 1300°C to be an optimal condition.<sup>26</sup> Data for the YSZ + Al<sub>2</sub>O<sub>3</sub> (0-7.5 wt%) samples sintered under these conditions (1300°C/8 h) are given in Table 3. Fired densities >99% ThD and shrinkages ≈25% were achieved. Density and grain size effects as a function of soak time were previously reported.<sup>5</sup>

Microstructures resulting from selected samples in Table 3 are shown in Figure 3 for polished and thermally etched sections of the YSZ + Al<sub>2</sub>O<sub>3</sub> (0-5.0 wt%) samples. Average grain sizes (0.2-0.3 μm) were equivalent, but the distribution was distinctly more bimodal for the higher content Al<sub>2</sub>O<sub>3</sub> samples. Also, there was an absence of twinning in any of the YSZ grains, an effect normally observed in martensitically transformed monoclinic grains. This could result from the small size of the grains or to the absence of a monoclinic phase.

Figure 3 also shows Al<sub>2</sub>O<sub>3</sub> inclusions as apparently discrete grains, of size equivalent to the YSZ grains, and fitting into the YSZ matrix with no obvious reaction zones. Lower magnification photomicrographs, however, revealed clustering of the Al<sub>2</sub>O<sub>3</sub> grains (Figure 4), the volume dispersion of the inclusions (dark areas in the photomicrographs) increasing with Al<sub>2</sub>O<sub>3</sub> content (0-5.0 wt%). Since the starting size of the Al<sub>2</sub>O<sub>3</sub> powder was 0.03 μm, it is evident that coalescence of the Al<sub>2</sub>O<sub>3</sub> particles must have occurred, either during the powder processing phase or as segregation of the Al<sub>2</sub>O<sub>3</sub> phase during sintering. The presence of discrete Al<sub>2</sub>O<sub>3</sub> grains in the 0.325 wt% Al<sub>2</sub>O<sub>3</sub>-YSZ microstructure (Figure 4b) also demonstrated the limited solubility of Al<sub>2</sub>O<sub>3</sub> in the YSZ structure.

Modulus of rupture data obtained on 4-point bend specimens are given in Figure 5 for the YSZ-Al<sub>2</sub>O<sub>3</sub> (0-7.5 wt%) composite samples. Data points for each composition represented the mean of ≈20 samples with a range of plus or

minus one standard deviation, as shown. Even with the spread in data points, the MOR values showed a clear trend towards higher values (from a base of  $\approx 270$  MPa for the YSZ sample) with increasing  $\text{Al}_2\text{O}_3$  content.

Fracture toughness data on the YSZ- $\text{Al}_2\text{O}_3$  composite samples are shown in Figure 6. As with the MOR data, a small maxima was present at 0.325 wt%  $\text{Al}_2\text{O}_3$ , ( $\approx 5.5 \text{ MPa}\cdot\text{m}^{1/2}$  up from  $4.5 \text{ MPa}\cdot\text{m}^{1/2}$  for the YSZ sample), followed by a more pronounced increase in the fracture toughness to  $\approx 9 \text{ MPa}\cdot\text{m}^{1/2}$  at 3.25 wt%  $\text{Al}_2\text{O}_3$ . The more pronounced effect of the  $\text{Al}_2\text{O}_3$  additions on the fracture toughness compared to the rupture modulus reflects the greater sensitivity of the measured MOR to flaws present in the tensile surface of the test specimens.

Evaluation of the expansion data showed a decrease in the thermal expansion coefficient (over the range from room temperature to  $1000^\circ\text{C}$ ) of the YSZ with increasing  $\text{Al}_2\text{O}_3$  additions. Calculated coefficients of thermal expansion were  $11.30 \times 10^{-6} \text{ }^\circ\text{C}^{-1}$  for the YSZ + 0.325 wt%  $\text{Al}_2\text{O}_3$  sample and  $10.73 \times 10^{-6} \text{ }^\circ\text{C}^{-1}$  for the 3.25 wt%  $\text{Al}_2\text{O}_3$  sample. This change would be expected for the composite material since  $\text{Al}_2\text{O}_3$  has a significantly lower thermal expansion ( $7.2 \times 10^{-6} \text{ }^\circ\text{C}^{-1}$ )<sup>27</sup> than the YSZ. No microcracking was observed around the  $\text{Al}_2\text{O}_3$  inclusions, which might have resulted from the tensile state of the surrounding YSZ matrix due to the thermal expansion mismatch.

Figure 7a shows a representative TEM photomicrograph (200kX) of the YSZ (base sample) grain boundary structure and triple point regions. The accompanying microdiffraction pattern in Figure 7b (obtained from the condensed beam condition) of the  $[111]$  axis shows the tetragonal-like structure of the grain, although a few grains were also indexed as cubic. The lack of full tetragonality is indicated by the fact that all the expected  $(211)$  diffraction spots were not present. Similar to Butler and Drennan,<sup>4</sup>

$\text{Al}_2\text{O}_3$  grains in the TEM samples (0.325 wt%  $\text{Al}_2\text{O}_3$ ) were found to contain relatively electron-opaque spherical inclusions of YSZ as illustrated in Figure 7c. The inclusions could be resolved and identified by EDS analysis to a high degree of confidence, since the beam diameter on the (Vacuum Generators HB5 Field Emission) STEM was  $\approx 0.5$  nm. TEM analysis of the  $\text{Al}_2\text{O}_3$  regions indicated the presence of "grain boundary dislocations" as illustrated in Figure 7d. This type of defect can be associated with the crystallographic mismatch ordinarily seen at grain boundaries. However, with the dislocation lines propagating some distance into the  $\text{Al}_2\text{O}_3$  grain this defect state is indicative of deformation occurring within the  $\text{Al}_2\text{O}_3$  grains in response to the strains generated in the YSZ matrix.<sup>22</sup>

Figure 8 shows representative EDS [STEM] spectra from YSZ grain centers (Figure 8a) and from triple point regions (Figures 8b, 8c and 8d) for the YSZ, 0.325 and 3.25 wt%  $\text{Al}_2\text{O}_3$  respectively. Data from the analysis of the spectra are collected in Table 4. For the composition ranges studied, the Zr content (wt%) remained relatively constant in the grain centers, but decreased in the triple points with increasing  $\text{Al}_2\text{O}_3$  additions. For Y, the trend noted was slightly increased concentration in the grain center with added  $\text{Al}_2\text{O}_3$  and little change in the triple point concentration. Taken together, the decrease of Zr in the triple point regions and increase of Y in the YSZ grains would suggest a stabilizing role for  $\text{Al}_2\text{O}_3$  in the YSZ structure.

The YSZ grains revealed only marginally detectable amounts of Al within the grains in line with the indicated low solubility of  $\text{Al}_2\text{O}_3$  in YSZ. In contrast, the Al concentration in the triple point regions increased significantly as the  $\text{Al}_2\text{O}_3$  content was increased. The level of Si detected was slightly higher than expected from the bulk spectrochemical analysis but within the accuracy of the EDS technique. The Si content in the triple

points also increased with added  $\text{Al}_2\text{O}_3$ , reflecting both a concentration of the impurities in the intergranular region and a greater affinity of  $\text{SiO}_2$  for  $\text{Al}_2\text{O}_3$  compared to  $\text{ZrO}_2$ .<sup>14</sup> The increased concentration of Si and Al in the triple point regions would indicate the formation of a more glassy intergranular phase with added  $\text{Al}_2\text{O}_3$ .

X-ray diffraction spectra from the sintered YSZ- $\text{Al}_2\text{O}_3$  composite samples (0, 0.325, 3.25, 5.0 wt%  $\text{Al}_2\text{O}_3$ ) are presented in Figure 9. The spectra show a small  $\alpha$ - $\text{Al}_2\text{O}_3$  (202) peak which increased with  $\text{Al}_2\text{O}_3$  content. Splitting of the lower intensity peaks [(200) and (311)] was evident in the spectra. The location of the peaks matched the multiplicity of crystallographic planes for a tetragonal phase [(002) peak intensity  $\cong \frac{1}{2}(200)$ ; (220)  $\cong \frac{1}{2}(202)$ ; (113)  $\cong \frac{1}{2}(311)$ ]. The x-ray data would indicate the presence of both cubic and tetragonal phases in the sintered specimens, a result which might be expected from the composition of the starting powders, since the phase diagram for the  $\text{Y}_2\text{O}_3$ - $\text{ZrO}_2$  system places the 4.5 mol% YSZ composition at 1300°C in the cubic-tetragonal solid solution phase field. However, the lack of discreteness between the (311) and (113) peaks, as well as the broadness of the peaks, suggest a continuum between the two phases rather than a mixture of discrete cubic and tetragonal grains.<sup>28</sup> This observation is supported by the TEM electron diffraction analysis, since the tetragonal patterns observed could be interpreted as emanating from distorted cubic grains. From the x-ray data, the relative amounts of cubic and tetragonal phases were estimated. This data is presented in Figure 10, which shows an apparent slight increase in the cubic phase (63 to 67 vol%) with added  $\text{Al}_2\text{O}_3$ , indicative of enhanced stabilization within the system and in agreement with the EDS observations.

The presence of the monoclinic phase was not detected by any of the above analytical techniques. This is supported by Raman spectra taken of the

polished, fired surfaces of 0, 0.325 and 3.25 wt%  $\text{Al}_2\text{O}_3$  specimens at room temperature and at 10 degrees Kelvin, as can be seen in Figure 11. The low-temperature data was obtained to facilitate possible monoclinic phase formation since the further a material is taken below its martensitic transformation temperature, the stronger is its tendency to transform.<sup>29</sup> The room temperature spectra for all specimens showed distinct tetragonal peaks as well as broader cubic peaks, in agreement with Benner and Nagelberg.<sup>30</sup> At low temperature, the cubic phase appeared to be more in evidence. No evidence of monoclinic phase was detected, either in the fracture or polished surfaces for compositions up to 3.25 wt%  $\text{Al}_2\text{O}_3$ . X-ray diffraction spectra of the fracture surfaces likewise did not reveal any trace of a monoclinic presence up to 7.5 wt%  $\text{Al}_2\text{O}_3$ . The fact that a monoclinic phase was not developed can be attributed to the small grain size (0.2 to 0.3  $\mu\text{m}$ ) as discussed by Matsui et al.<sup>21</sup>

From the x-ray diffraction data (Figure 9), lattice parameter values were calculated as a function of  $\text{Al}_2\text{O}_3$  content (0-7.5 wt%). These data are presented in Table 5, which gives the c and a lattice parameters, c/a ratios, cell volume, V, and equivalent cubic lattice parameter,  $a_0$ , as well as the  $a_0$  values calculated from the (111) peaks. A plot of these lattice parameter changes as a function of  $\text{Al}_2\text{O}_3$  content is given in Figure 12. The lattice parameter showed an initial decrease, which is consistent with the substitution of the smaller  $\text{Al}^{3+}$  for  $\text{Zr}^{4+}$  ions in the structure. However, the absolute solubility of  $\text{Al}_2\text{O}_3$  in 4.5 mol% YSZ remains unresolved as the x-ray powder diffraction data did not exhibit a clear region within which the lattice parameter did not change. The presence of discrete  $\text{Al}_2\text{O}_3$  grains in the microstructure at 0.325 wt%  $\text{Al}_2\text{O}_3$  content would indicate, however, that the solubility limit achieved was below this level.

Figure 13 gives dc conductivity data for the YSZ- $\text{Al}_2\text{O}_3$  samples over the

temperature range 25–800°C. The curves show two distinct slopes above and below approximately 100°C. In the lower temperature regions, no differences were detected in conductivity between the different samples, attributable to predominately electronic conduction in this region. However, above 100°C, where ionic conductivity would be expected to predominate, the conductivity first increased then progressively decreased with  $\text{Al}_2\text{O}_3$  content, as depicted in Figure 14, with a maximum occurring for the 0.325 wt%  $\text{Al}_2\text{O}_3$  sample. The observed increase (one-half order of magnitude) in conductivity with temperature for this sample is consistent with the limited solubility mechanism proposed since the associated defect-substitution of  $\text{Al}^{3+}$  for  $\text{Zr}^{4+}$  would result in increased  $\text{O}^{2-}$  vacancies and higher oxygen ion mobility. The subsequent decrease in conductivity is consistent with the increased presence of interstitial cations and discrete  $\text{Al}_2\text{O}_3$  grains, both of which might be expected to have a deleterious effect on oxygen ion mobility. In line with these observations, calculated activation energies from Figure 13 were approximately 0.9–1.0 eV for the ionic conduction range and 0.46 eV for the range below 100°C.

The absence of a monoclinic phase in the composite  $\text{YSZ-Al}_2\text{O}_3$  specimens, as determined by the various analytical techniques used in this investigation, would indicate that transformation toughening does not play a role in the increased strength and fracture toughness observed. Enhanced strength in the unmodified YSZ samples, relative to the cubic  $\text{YSZ}^{31}$  must be attributed, therefore, to the small grain size (0.2–0.3  $\mu\text{m}$ )<sup>32</sup> and presence of a tetragonal phase in the structure.

With  $\text{Al}_2\text{O}_3$  added, results showed discrete  $\text{Al}_2\text{O}_3$  grains within the composite matrix, deformation within these grains, and a decrease in  $\text{Y}_2\text{O}_3$  content in the intergranular phase, indicative of enhanced phase stability within the system. The role of the  $\text{Al}_2\text{O}_3$  in strengthening the composite

samples would seem to be: 1) in presenting a barrier to crack propagation by crack deflection around the dispersed, high modulus second phase, and 2) crack arrest mechanisms associated with deformation within the  $\text{Al}_2\text{O}_3$  grains. Support for this interpretation is given in Figure 15 which shows SEM photomicrographs of crack deflection around included  $\text{Al}_2\text{O}_3$  grains within the YSZ (5 wt%  $\text{Al}_2\text{O}_3$ ) composite structure. The cracks were generated from indentations made during the  $K_{Ic}$  evaluations.

#### IV. Conclusions

1) Additions of up to 7.5 wt%  $\text{Al}_2\text{O}_3$  (of equivalent particle size) to 4.5 mol% yttria-stabilized zirconia (YSZ) resulted in accelerated densification. Microstructures obtained consisted of well dispersed  $\text{Al}_2\text{O}_3$  inclusions in the 0.2 to 0.4  $\mu\text{m}$  grain size YSZ matrix.

2) Noticeable increases in the modulus of rupture and  $K_{Ic}$  values were obtained with  $\text{Al}_2\text{O}_3$  additions, maximally in the 3 to 5 wt% range.

3) X-ray diffraction and Raman spectroscopy data revealed the presence of approximately 35 vol% tetragonal phase which decreased slightly but remained essentially stable with added  $\text{Al}_2\text{O}_3$ . The presence of a monoclinic phase was not detected in either the polished or fracture surfaces of the sintered specimens.

4) Mechanical strengthening of the YSZ- $\text{Al}_2\text{O}_3$  composites was attributed to a combination of small grain size, the presence of the tetragonal phase, and the discrete  $\text{Al}_2\text{O}_3$  inclusions presenting a barrier to crack propagation. Transformation toughening does not appear to have contributed to the strengthening.

5) DC conductivity data indicated enhanced ionic conductivity with less than 3.25 wt%  $\text{Al}_2\text{O}_3$  added.

## V. Acknowledgments

This work was supported by the Office of Naval Research under contract No. N-00014-80-K-0969 and in part by the National Science Foundation under MRL grant No. DMR-80-20250. Thanks are due to W. M. Kriven and P. M. Mochel for assistance with TEM and STEM work, to Dean Levi for running the Raman specimens, and to M. K. Ferber for helpful conversations.

## VI. References

1. R. A. Youshaw and J. W. Halloran, "Compaction of Spray-Dried Powders," Am. Ceram. Soc. Bull. 61 [2] 227-230 (1982).
2. C. E. Scott and J. S. Reed, "Effect of Laundering and Milling on the Sintering Behavior of Stabilized Zirconia Powders," J. Am. Ceram. Soc. 58 [6] 587-590 (1979).
3. K. S. Mazdiyasi, C. T. Lynch, and J. S. Smith II, "Cubic Phase Stabilization of Translucent Yttria-Zirconia at Very Low Temperatures." J. Am. Ceram. Soc. 50 [10] 532-537 (1967).
4. D. M. Wilson, Effect of Aluminum and Boron Oxides on the Densification of Yttria-Stabilized Zirconia, Thesis, University of Illinois, (1983).
5. R. C. Buchanan and D. M. Wilson, "Role of  $Al_2O_3$  in Sintering of Submicrometer Yttria-Stabilized  $ZrO_2$  Powders," pp 526-540, Advances in Ceramics, Vol 10 Ed., W. D. Kingery, The American Ceramic Society, Columbus, Ohio, (1984).
6. H. Bernard, Microstructure et Conductivité de la Zircone Stabilisée Fritée, Ph. D. Thesis, Institut National Polytechnique de Grenoble, (1980).
7. R. W. Rice and R. C. Pohanka, "Grain Size Dependence of Spontaneous Cracking in Ceramics," J. Am. Ceram. Soc. 62 [11-12] 559-563 (1979).
8. A. J. A. Winnubst, K. Keizer and A. J. Burggraaf, "Mechanical Properties and Fracture Behavior of  $ZrO_2$ - $Y_2O_3$  Ceramics," J. of Mater. Sci. 18 1958-66 (1983).
9. S. Wu and R. J. Brook, "Sintering Additives for  $ZrO_2$  Ceramics," Trans. Br. Cer. Soc. 82 200-5 (1983).
10. J. E. Burke, "Sintering and Microstructure Control," G. E. Report 68-C-368, (1968).
11. M. F. Yan, R. M. Cannon, H. K. Bowen and R. L. Coble, "Space-Charge Contribution to Grain-Boundary Diffusion," J. Am. Ceram. Soc. 60 [3-4] 120-7 (1977).
12. W. D. Kingery, "Plausible Concepts Necessary and Sufficient for Interpretation of Ceramic Grain Boundary Phenomina: II, Solute Segregation, Grain Boundary Diffusion and General Discussion," J. Am. Ceram. Soc. 57 [2] 74-83 (1974).
13. M. F. Yan, R. M. Cannon and H. K. Bowen, "Effect of Grain Size Distribution on Sintered Density," Mater. Sci. and Eng. 60 275-81 (1983).

14. E. P. Butler and J. Drennan, "Microstructural Analysis of Sintered High-Conductivity Zirconia with  $Al_2O_3$  Additions," J. Am. Ceram. Soc. **65** [10] 474-478 (1982).
15. N. M. Berkman, L. Heyne, "Correlation Between Impedance, Microstructure and Composition of CSZ," Electrochim Acta **21**, [4] 303-10 (1976).
16. N. Claussen and M. Rühle, "Design of Transformation-Toughened Ceramics," pp137-163, The Science and Technology of Zirconia, Advances in Ceramics, Vol. 3, Ed. A. H. Heuer and L. W. Hobbs, The American Ceramic Society, Columbus, Ohio (1981).
17. C. M. Wayman, "Martinsitic Transformations," pp64-81 *ibid.*
18. W. M. Kriven, W. L. Fraser and S. W. Kennedy, "The Martinsite Crystallography of Tetragonal Zirconia," pp82-97, *ibid.*
19. K. T. Faber, "Microcracking Contributions to the Toughness of  $ZrO_2$ -Based Ceramics," pp293-305, The Science and Technology of Zirconia II, Advances in Ceramics, Vol. 12, The American Ceramic Society, Columbus, Ohio (1984).
20. K. Tsukuma, K. Ueda and M. Shimada, "Strength and Fracture Toughness of Isostatically Hot-Pressed Composites of  $Al_2O_3$  and a  $Y_2O_3$ -Partially-Stabilized  $ZrO_2$ ," J. Am. Ceram. Soc. **68** [1] C4-C5 1985.
21. M. Matsui, T. Soma and I. Oda, "Effect of Microstructure on the Strength of Y-TZP Components," pp371-381, The Science and Technology of Zirconia II, Advances in Ceramics, Vol. 12, The American Ceramic Society, Columbus, Ohio (1984).
22. B. V. Narashimha Rao, "Accommodation Substructure in the  $\alpha Al_2O_3$  of a PSZ," GM Res. Lab Tech. Rept #3533.
23. K. Niihara, R. Morena and D. P. H. Hasselman, "Evaluation of  $K_{IC}$  of Brittle Solids by the Indentation Method with Low Crack-to-Indent Ratios," J. Mater. Sci. Lett. **1** 13-16 (1982).
24. G. R. Anstis, P. Chantikul, B. R. Lawn and D. B. Marshall, "A Critical Evaluation of Indentation Techniques for \*measuring Fracture Toughness: I, Direct Crack Measurements," J. Am. Ceram. Soc. **64** [9] 533-538 (1981).
25. M. I. Mendelsohn, "Average Grain Size in Polycrystalline Ceramics," J. Am. Ceram. Soc. **52** [8] 443-6 (1969).
26. W. W. Davison, Influence of Alumina on Structural and Mechanical Properties of Yttria-Stabilized Zirconia, p 52; M.S. Thesis, University of Illinois (1985).
27. W. J. Lackey, D. P. Stinton, G. A. Cerny, L. L. Fehrenbacher and A. C. Schaffhauser, "Ceramic Coatings for Heat Engine Materials - Status and Future Needs," Proceedings of International Symposium on Ceramic Components for Heat Engines, October 17-21, 1983, Hakone, Japan.
28. A. Feinberg and C. H. Perry, "Structural Disorder and Phase in  $ZrO_2$ - $Y_2O_3$  System," J. Phys. Chem. Solids **42** 513-518 (1981).

29. P. F. Becher, M. V. Swain and M. K. Ferber, "Relation of Transformation Temperature to the Fracture Toughness of Transformation Toughened Ceramics," submitted for publication to the J. of Mater. Sci.
30. R. E. Benner and H. S. Nagelberg, "Characterization of  $ZrO_2$ - $Y_2O_3$  Thermal Barrier Coatings by Raman Spectroscopy," Thin Solid Films **84** pp89-94 (1981).
31. Ceramic Source '86, p 346, The American Ceramic Society, Columbus, OH (1985).
32. R. W. Rice, "Strength/Grain-Size Effects in Ceramics," Proc. Br. Ceram. Soc. **20** 205-257 (1972).

Table 1  
YSZ and Al<sub>2</sub>O<sub>3</sub> Precursor Properties

---

YSZ*	8 wt% Y <sub>2</sub> O <sub>3</sub>				
	Average Particle Size: 0.03 μm				
	Surface Area: 50 m <sup>2</sup> /gm				
	Crystalline Phase: Cubic				
	Impurities >0.02 wt%:				
		<u>wt%</u>		<u>wt%</u>	
	HfO <sub>2</sub>	1.6	H <sub>2</sub> O	2.2	
	Al <sub>2</sub> O <sub>3</sub>	0.2	Cl	1.0	
	CaO	0.3	Na <sub>2</sub> O	0.3	
	MgO	0.1	SiO <sub>2</sub>	0.1	

---

\* Zircar Corp, Florida, N. Y.

Table 2  
Properties of Alumina Powders and Additive Effects to YSZ

Alumina Precursor	Avg. P.S.	Amounts Added	Microstructure	Effects on
A) Al(OH) <sub>3</sub> Powder* (calcined)	0.05, 10 μm (Bi-modal)	0-3.25 wt%		Large inclusions with porosity, otherwise dense
B) Al <sub>2</sub> (C <sub>2</sub> O <sub>4</sub> ) <sub>3</sub> ** (Oxalate)	0.10 μm	0.325 wt%		Some porosity present
C) Al(OH) <sub>3</sub> Gel** (calcined)	0.05 μm	0.325 wt%		Samples dense
D) Al <sub>2</sub> O <sub>3</sub> 0.03 μm <sup>†</sup> Floated powder	0.03 μm	0-7.5 wt%		Samples dense, even at low psi pressing

\* J.T. Baker Chemical Co., Phillipsburg, NJ  
 \*\* Pfaltz and Bauer, Inc., Stamford, CT  
 † Apache Chemicals, Inc., Seward, IL

Table 3  
Sintered Data for YSZ + Al<sub>2</sub>O<sub>3</sub> Samples

---

Sample				Diametrical
<u>Composition</u>	<u>Green Density</u>	<u>ThD</u>	<u>Fired ThD</u> <sup>a</sup>	<u>Shrinkage</u>
(wt% Al <sub>2</sub> O <sub>3</sub> )	(g/cm <sup>3</sup> )	(g/cm <sup>3</sup> )	%	%
0.0	2.54	6.04	98.3	25.0
0.325	2.55	5.99	99.7	26.4
0.65	2.55	5.98	98.7	24.6
1.3	2.55	5.93	98.5	25.4
3.25	2.55	5.83	99.1	25.7
5.0	2.43	5.81	98.5	25.2
7.5	2.39	5.74	95.9	25.8

---

<sup>a</sup> Sintering Temperature/Time: 1300°C/8 h

Table 4  
 EDS Elemental Analysis of Grain Centers  
 and Triple Points from YSZ-Al<sub>2</sub>O<sub>3</sub> TEM Specimens

<u>Sample/Location</u>	<u>wt%</u>			
	<u>Zr</u>	<u>Y</u>	<u>Si</u>	<u>Al</u>
YSZ Grain	90.9	8.4	0.5	0.2
Tr Pt	84.6	12.6	2.1	0.7
0.325 Grain	90.3	8.8	0.7	0.2
Tr Pt	84.0	12.9	2.2	0.9
3.25 Grain	89.7	9.1	0.9	0.3
Tr Pt	82.5	13.1	2.5	1.9

accuracy  $\approx$  1.0 %

Table 5  
Lattice parameters Derived from X-Ray Diffraction  
of YSZ-Al<sub>2</sub>O<sub>3</sub> Composite System

Composition (wt % Al <sub>2</sub> O <sub>3</sub> )	<u>c</u> (nm)	<u>a</u> (nm)	<u>(c/a)</u>	<u>v</u> (nm) <sup>3</sup>	<u>a<sub>o</sub></u> <sup>*</sup> (nm)	<u>a<sub>o</sub>(111)</u> <sup>**</sup> (nm)
0	0.51488	0.51108	1.0074	0.1345	0.51234	0.51425
0.325	0.51526	0.50980	1.0107	0.1339	0.51161	0.51130
0.65	0.51484	0.51012	1.0093	0.1340	0.51169	0.51177
1.3	0.51648	0.51060	1.0115	0.1346	0.51255	0.51255
3.25	0.51746	0.51174	1.0112	0.1345	0.51364	0.51381
5.0	0.51704	0.51064	1.0125	0.1348	0.51276	0.51291
7.5	0.51690	0.51074	1.0121	0.1348	0.51279	0.55284

\* a<sub>o</sub> calculated from unit cell volume

\*\* a<sub>o</sub> calculated from (111) peaks

## List of Figures

- Figure 1. SEM photomicrographs of as received YSZ (A) and 0.03  $\mu\text{m}$  float  $\text{Al}_2\text{O}_3$  powders (B) showing morphology and agglomerate structure.
- Figure 2. Densification behavior for YSZ +  $\text{Al}_2\text{O}_3$ (0.0325 wt%) sample as a function of soak temperature and time at 1200-1350°C for 0.5 to 24 h.
- Figure 3. SEM photomicrographs of polished and thermally etched sections of ( $\text{YSZ} + \text{Al}_2\text{O}_3$ ) samples (1300°C/8 h), showing grain size distribution and  $\text{Al}_2\text{O}_3$  inclusions (dark areas): (A) YSZ, (B) YSZ +  $\text{Al}_2\text{O}_3$ (0.325 wt%), (C) YSZ +  $\text{Al}_2\text{O}_3$ (3.25 wt%), (D) YSZ +  $\text{Al}_2\text{O}_3$ (5.0 wt%)
- Figure 4. Lower magnification SEM photomicrographs of the samples in Figure 3, showing dispersion of  $\text{Al}_2\text{O}_3$  grains in the YSZ- $\text{Al}_2\text{O}_3$  composite.
- Figure 5. Plot of MOR as a function of added  $\text{Al}_2\text{O}_3$  content (0-7.5 wt%) for YSZ- $\text{Al}_2\text{O}_3$  composites.
- Figure 6. Plot of fracture toughness as a function of added  $\text{Al}_2\text{O}_3$  content (0-7.5 wt%) for YSZ- $\text{Al}_2\text{O}_3$  composites.
- Figure 7. TEM photomicrographs of YSZ- $\text{Al}_2\text{O}_3$  composite samples: (A) representative photomicrograph of YSZ base sample showing grain boundary and triple point regions, (B) Electron microdiffraction pattern of typical YSZ grain [111] axis showing tetragonal-like structure, (C) YSZ spherical inclusions in YSZ +  $\text{Al}_2\text{O}_3$ (3.25 wt%), (D)  $\text{Al}_2\text{O}_3$  grain with internal and grain boundary dislocations.
- Figure 8. EDS (STEM) spectra of the YSZ- $\text{Al}_2\text{O}_3$  samples representing: (A) YSZ grain center, (B) YSZ triple point, (C) triple point in YSZ +  $\text{Al}_2\text{O}_3$ (0.325 wt%), (D) triple point in YSZ +  $\text{Al}_2\text{O}_3$ (3.25 wt%)
- Figure 9. X-Ray diffraction spectra of YSZ +  $\text{Al}_2\text{O}_3$ (0, 0.325, 3.25 and 5.0 wt%) samples. Splitting of the major peaks indicates combined tetragonal and cubic phases.

- Figure 10. Estimated volume fraction of cubic phase in 0-7.5 wt%  $\text{Al}_2\text{O}_3$ -YSZ.
- Figure 11. Raman spectra of YSZ +  $\text{Al}_2\text{O}_3$  (0, 0.325, 3.25 wt%) at (A) 298°K and (B) 10°K showing primarily tetragonal and also cubic peaks.
- Figure 12. Lattice parameter changes in the YSZ- $\text{Al}_2\text{O}_3$  samples as a function of added  $\text{Al}_2\text{O}_3$  content
- Figure 13. DC conductivity of YSZ- $\text{Al}_2\text{O}_3$  samples as a function of reciprocal temperature
- Figure 14. Variation of dc conductivity with added  $\text{Al}_2\text{O}_3$  to YSZ at 600°C and 450°C for 0-7.5 wt%  $\text{Al}_2\text{O}_3$ .
- Figure 15. SEM photomicrographs of YSZ + 5.0 wt%  $\text{Al}_2\text{O}_3$  at (A) 4.09 kX and (B) 12.4 kX magnification showing crack deflection of indentation induced cracking around included  $\text{Al}_2\text{O}_3$  grains.

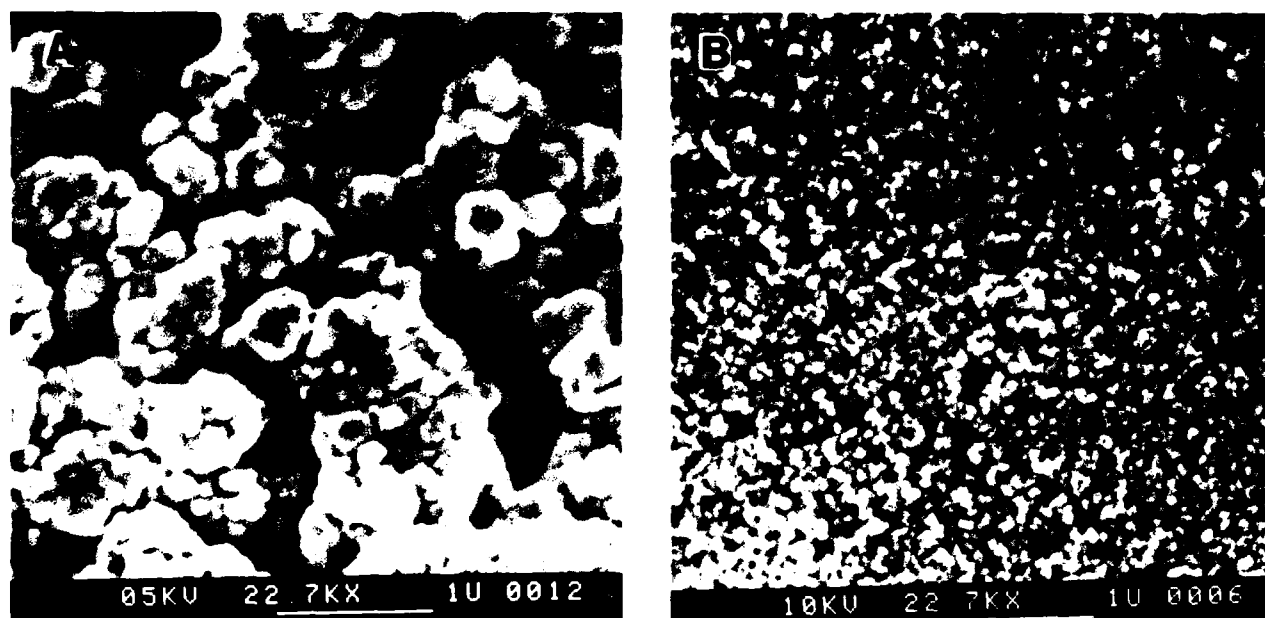


Figure 1. SEM photomicrographs of as received YSZ (A) and 0.03 μm float Al<sub>2</sub>O<sub>3</sub> powders (B) showing morphology and agglomerate structure.

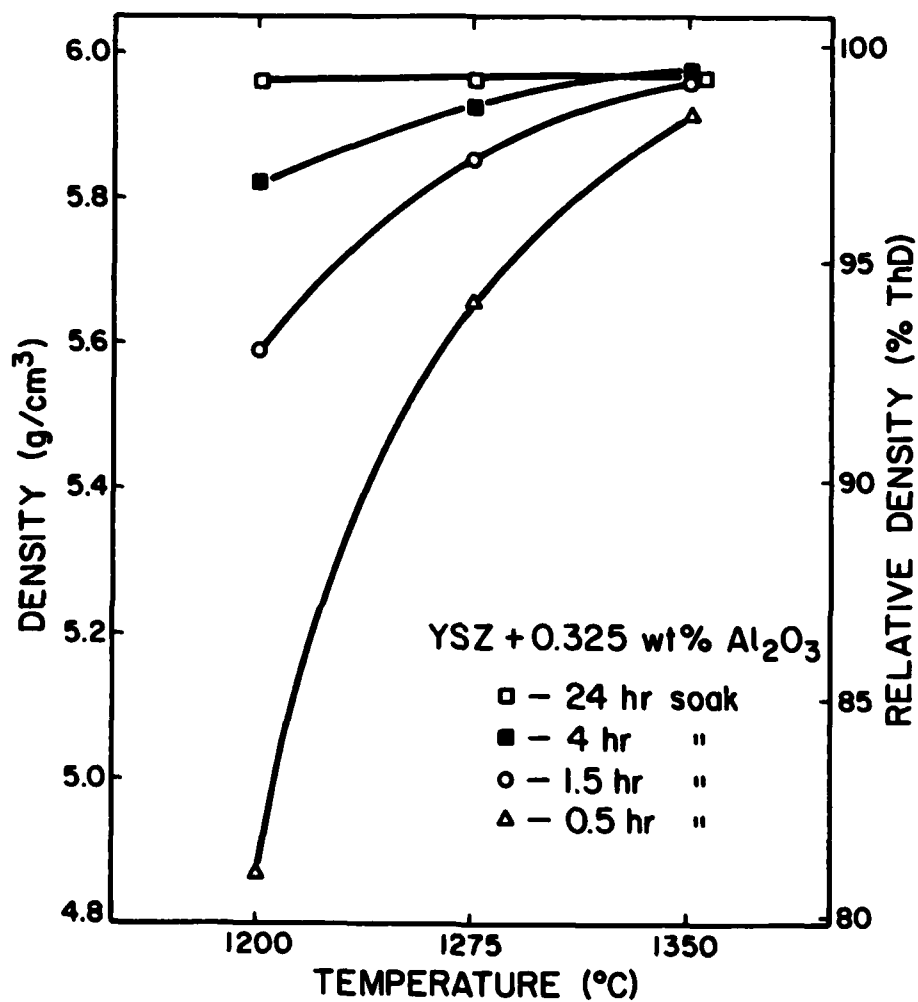


Figure 2. Densification behavior for YSZ + Al<sub>2</sub>O<sub>3</sub> (0.0325 wt%) sample as a function of soak temperature and time at 1200-1350°C for 0.5 to 24 h.

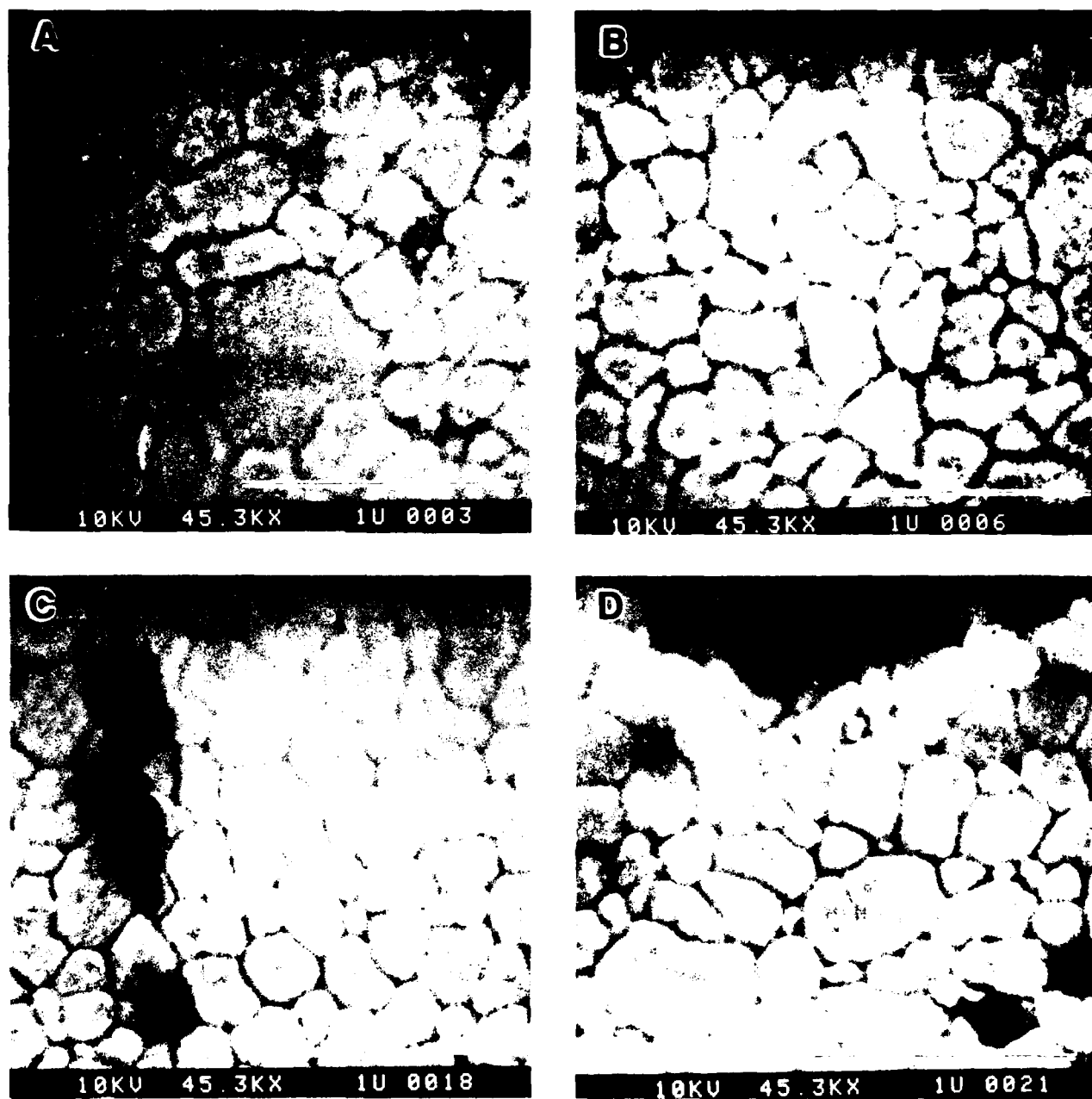


Figure 3. SEM photomicrographs of polished and thermally etched sections of (YSZ + Al<sub>2</sub>O<sub>3</sub>) samples (1300°C/8 h), showing grain size distribution and Al<sub>2</sub>O<sub>3</sub> inclusions (dark areas): (A) YSZ, (B) YSZ + Al<sub>2</sub>O<sub>3</sub> (0.325 wt%), (C) YSZ + Al<sub>2</sub>O<sub>3</sub> (3.25 wt%), (D) YSZ + Al<sub>2</sub>O<sub>3</sub> (5.0 wt%)

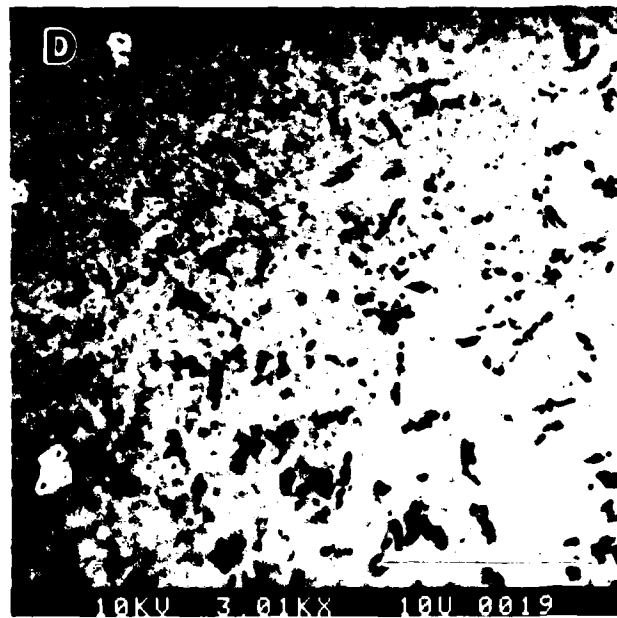
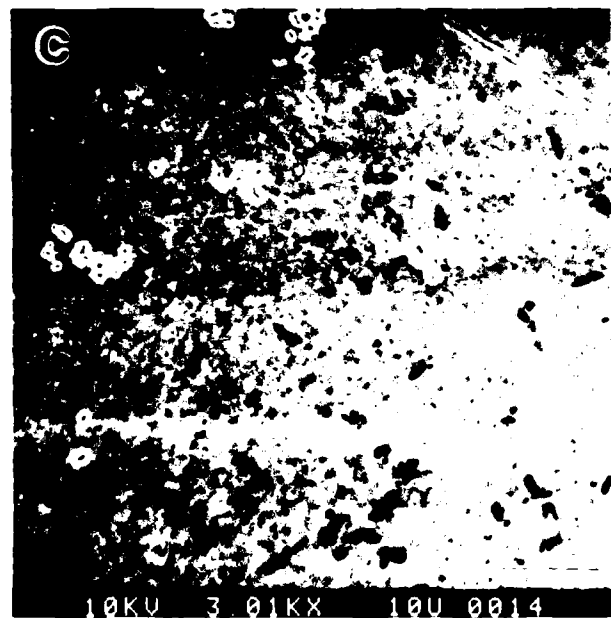
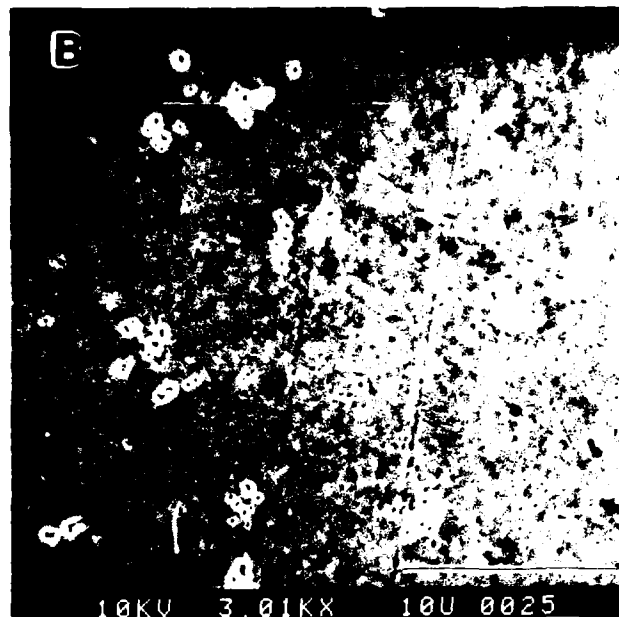
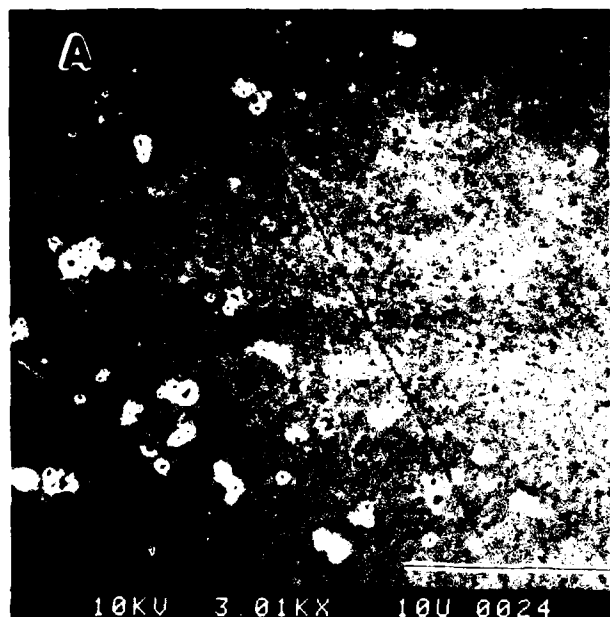


Figure 4. Lower magnification SEM photomicrographs of the samples in Figure 3, showing dispersion of  $\text{Al}_2\text{O}_3$  grains in the YSZ- $\text{Al}_2\text{O}_3$  composite.

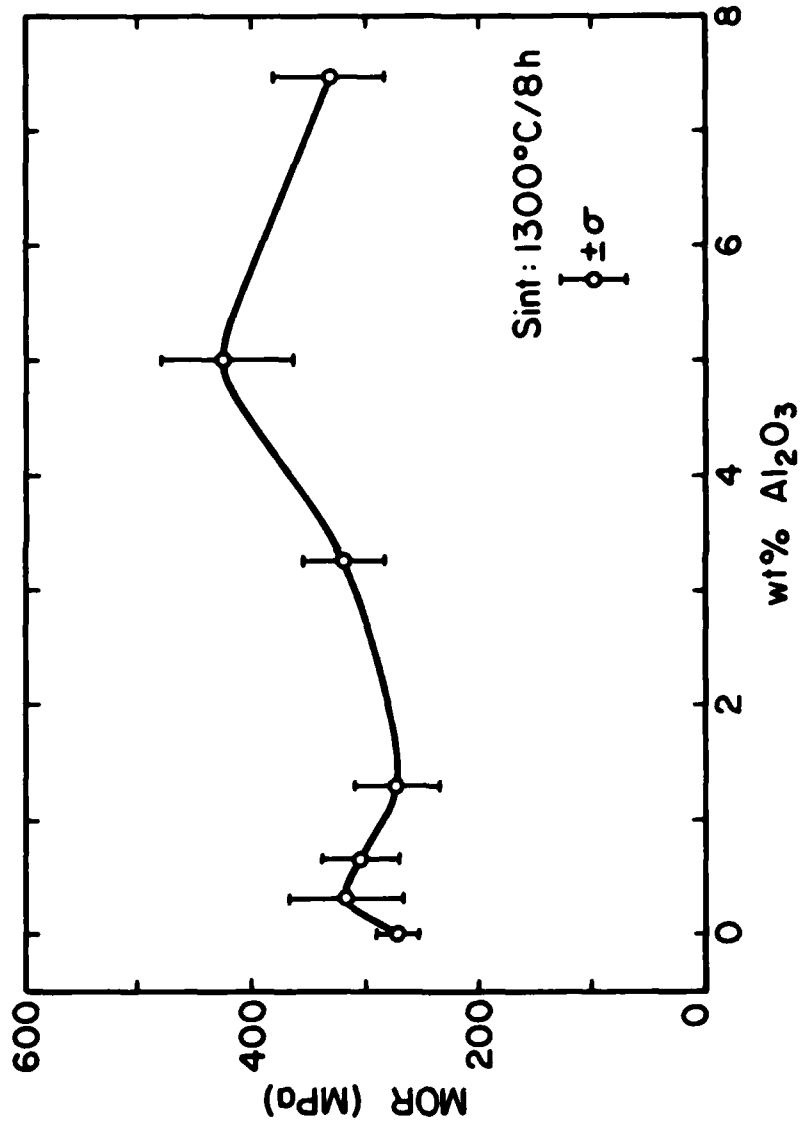


Figure 5. Plot of MOR as a function of added Al<sub>2</sub>O<sub>3</sub> content (0-7.5 wt%) for YSZ-Al<sub>2</sub>O<sub>3</sub> composites.

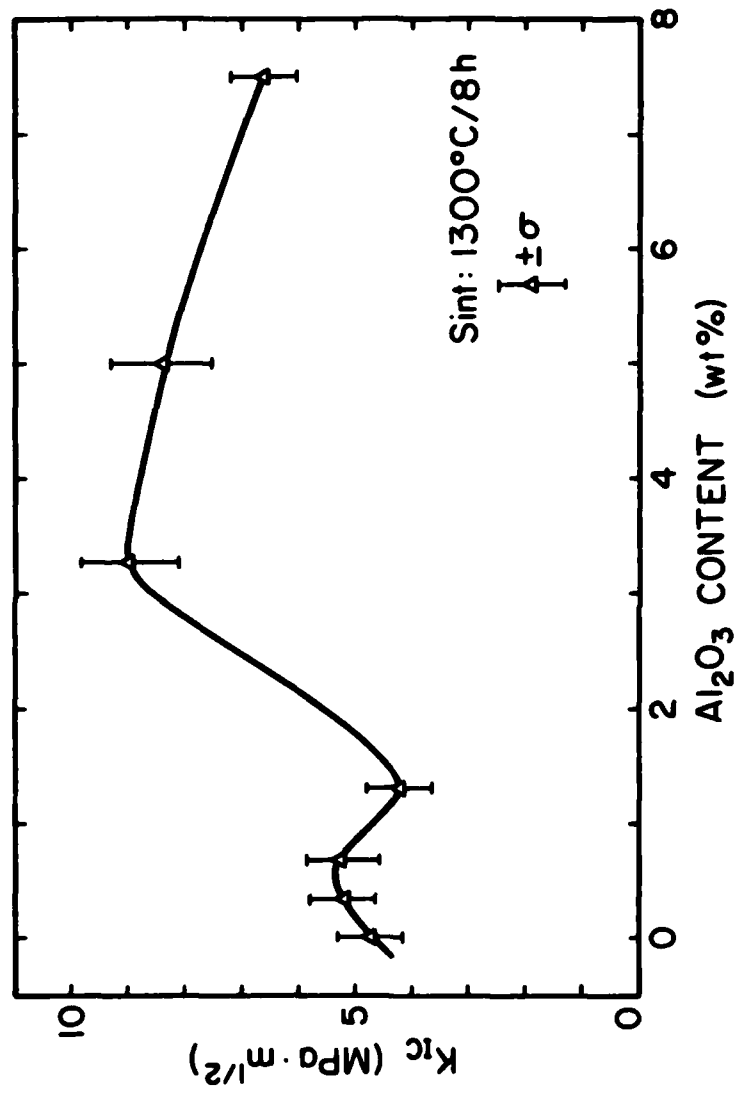


Figure 6. Plot of fracture toughness as a function of added  $\text{Al}_2\text{O}_3$  content (0-7.5 wt%) for YSZ- $\text{Al}_2\text{O}_3$  composites.

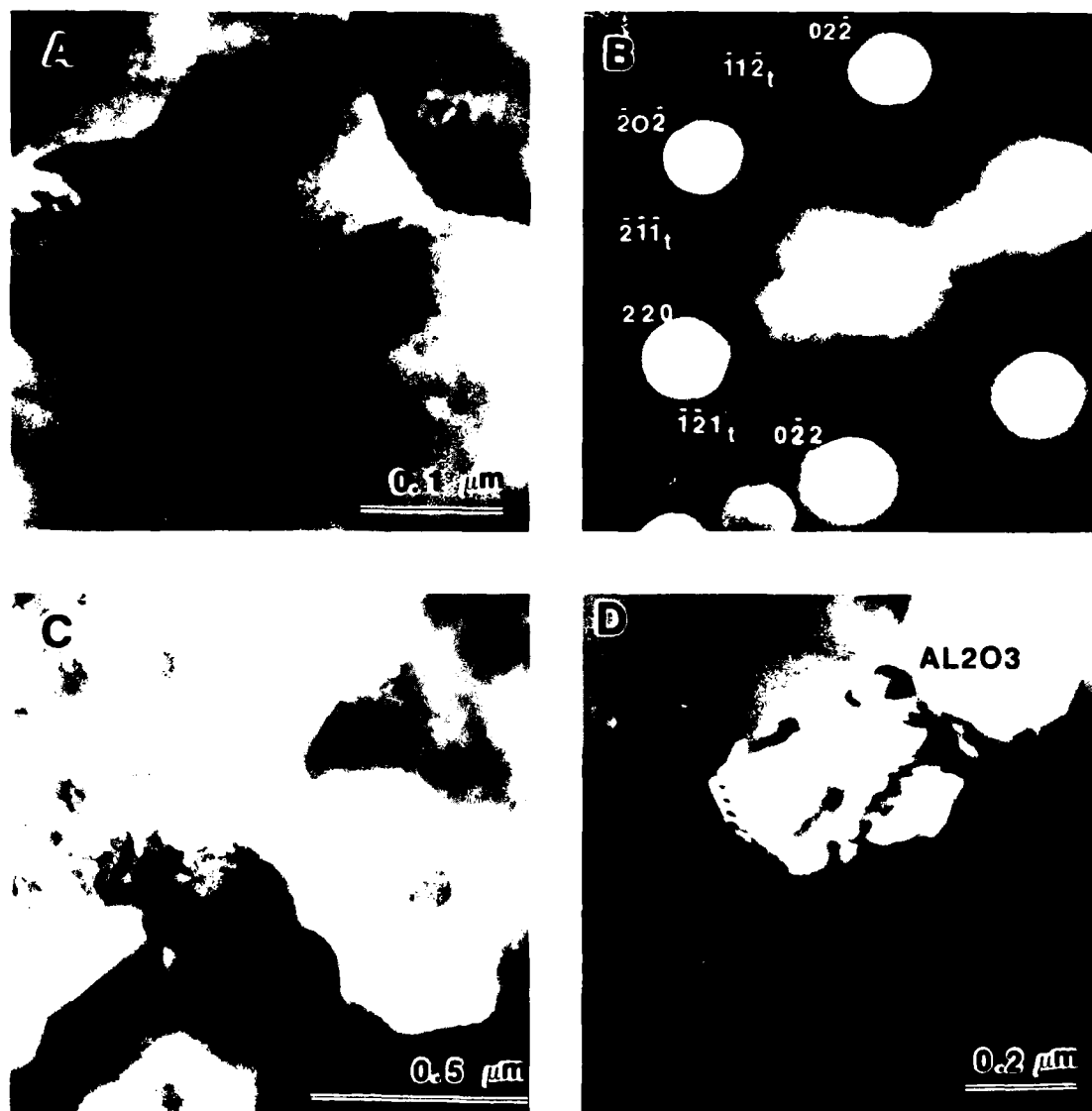


Figure 7. TEM photomicrographs of YSZ- $\text{Al}_2\text{O}_3$  composite samples: (A) representative photomicrograph of YSZ base sample showing grain boundary and triple point regions, (B) Electron microdiffraction pattern of typical YSZ grain [111] axis showing tetragonal-like structure, (C) YSZ spherical inclusions in YSZ +  $\text{Al}_2\text{O}_3$  (3.25 wt%), (D)  $\text{Al}_2\text{O}_3$  grain with internal and grain boundary dislocations.

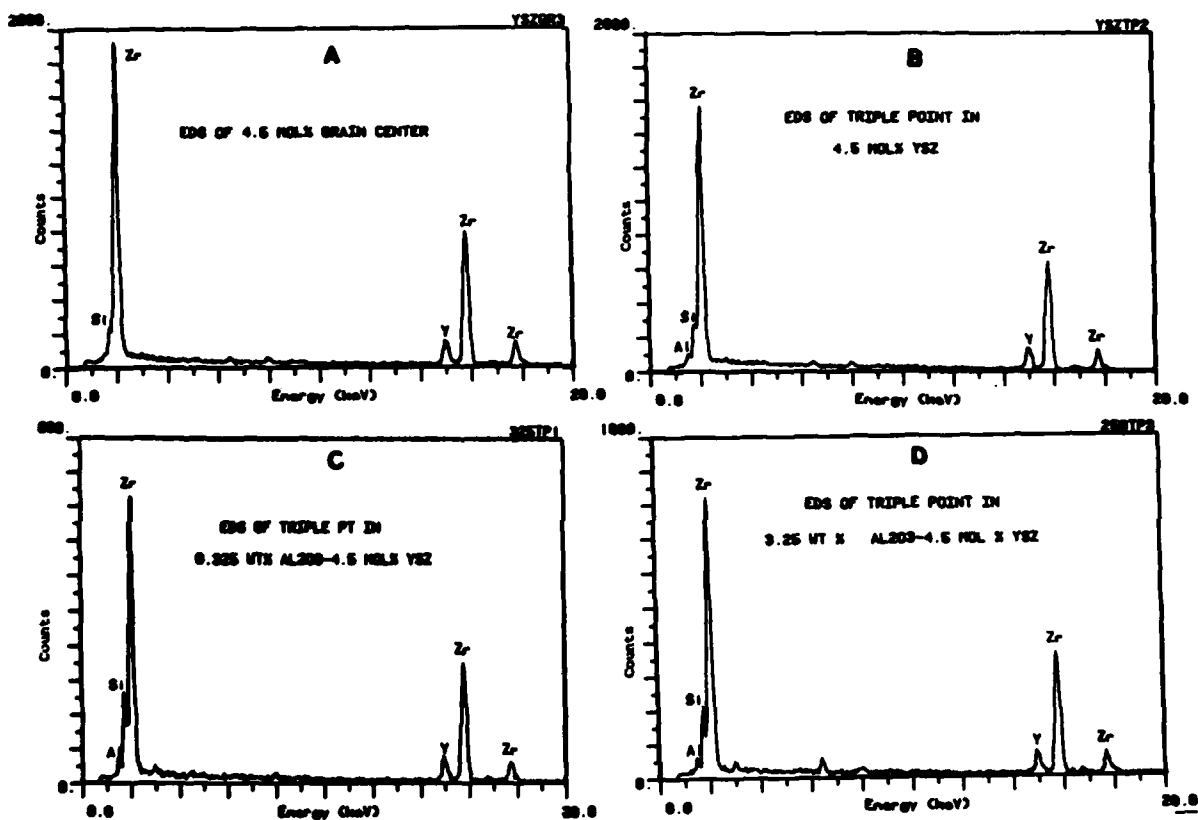


Figure 8. EDS (STEM) spectra of the YSZ- $\text{Al}_2\text{O}_3$  samples representing: (A) YSZ grain center, (B) YSZ triple point, (C) triple point in YSZ +  $\text{Al}_2\text{O}_3$  (0.325 wt%), (D) triple point in YSZ +  $\text{Al}_2\text{O}_3$  (3.25 wt%)

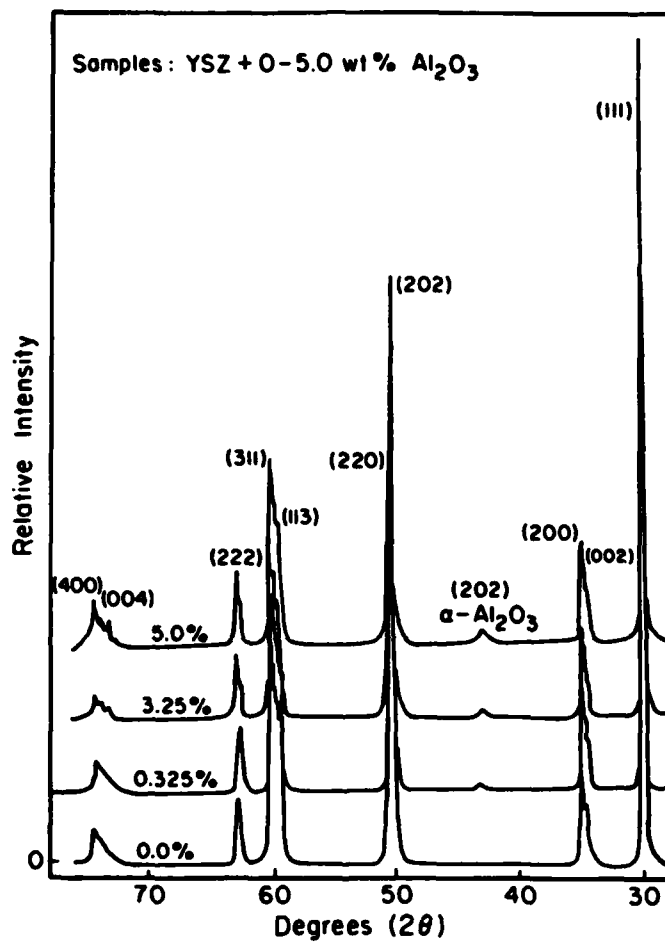


Figure 9. X-Ray diffraction spectra of YSZ +  $\text{Al}_2\text{O}_3$  (0, 0.325, 3.25 and 5.0 wt%) samples. Splitting of the major peaks indicates combined tetragonal and cubic phases.

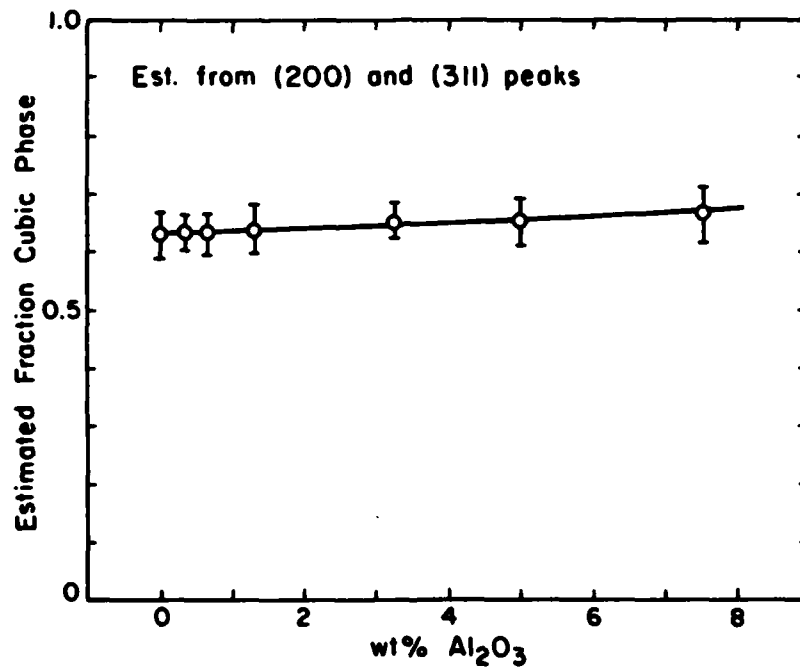


Figure 10. Estimated volume fraction of cubic phase in 0-7.5 wt%  $\text{Al}_2\text{O}_3$ -YSZ.

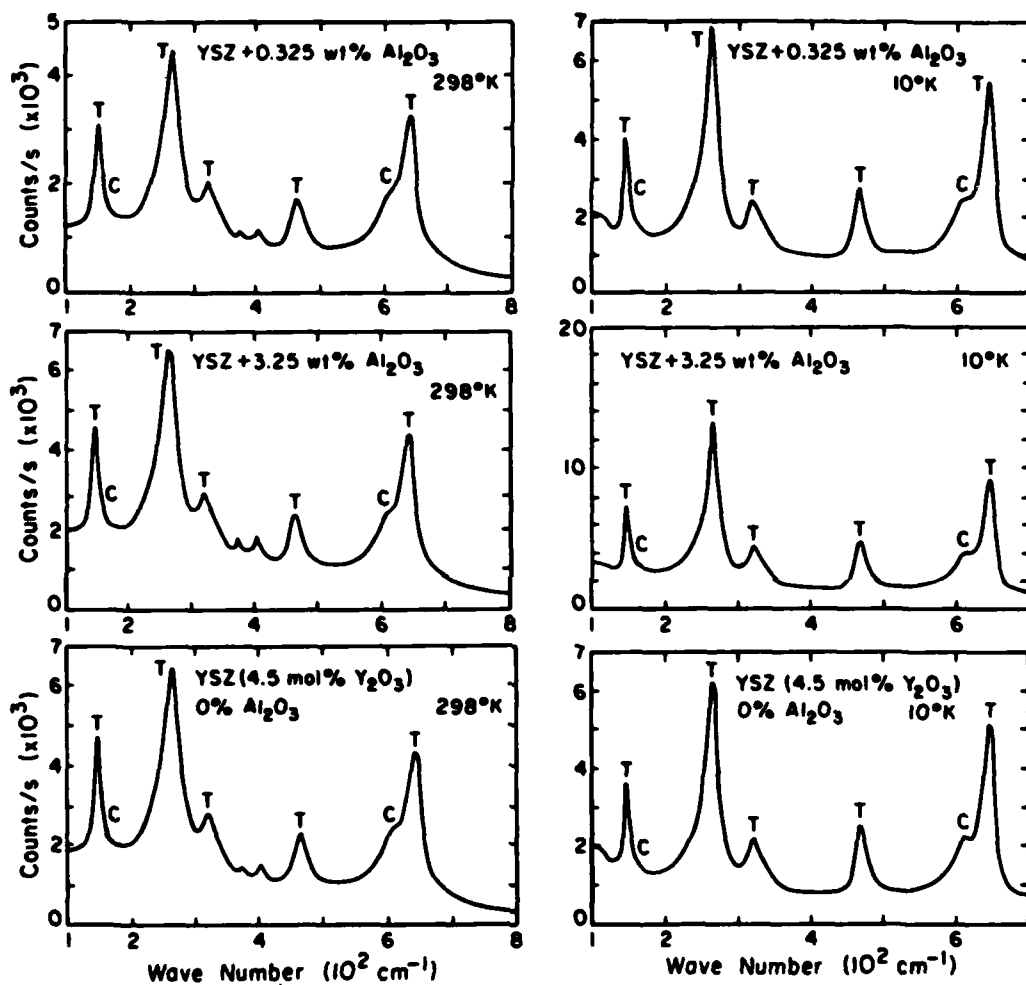


Figure 11. Raman spectra of YSZ + Al<sub>2</sub>O<sub>3</sub> (0, 0.325, 3.25 wt%) at (A) 298°K and (B) 10°K showing primarily tetragonal and also cubic peaks.

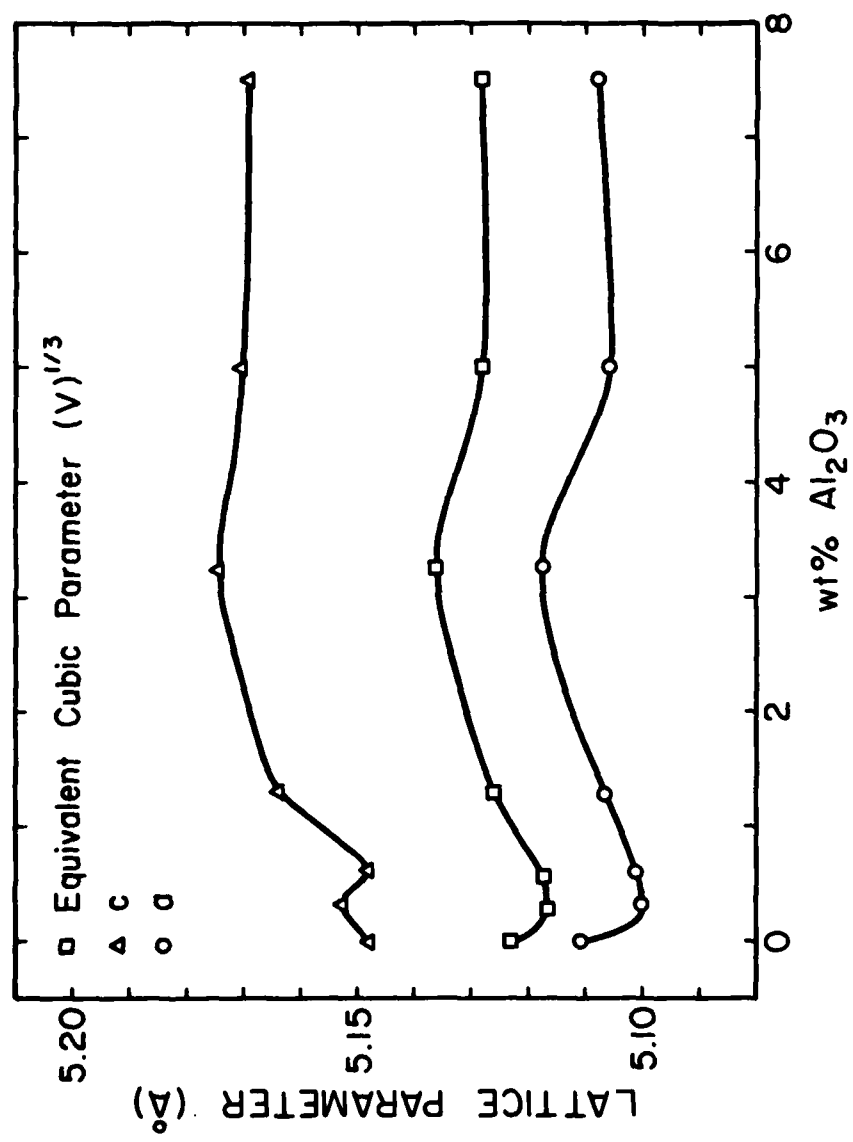


Figure 12. Lattice parameter changes in the YSZ-Al<sub>2</sub>O<sub>3</sub> samples as a function of added Al<sub>2</sub>O<sub>3</sub> content

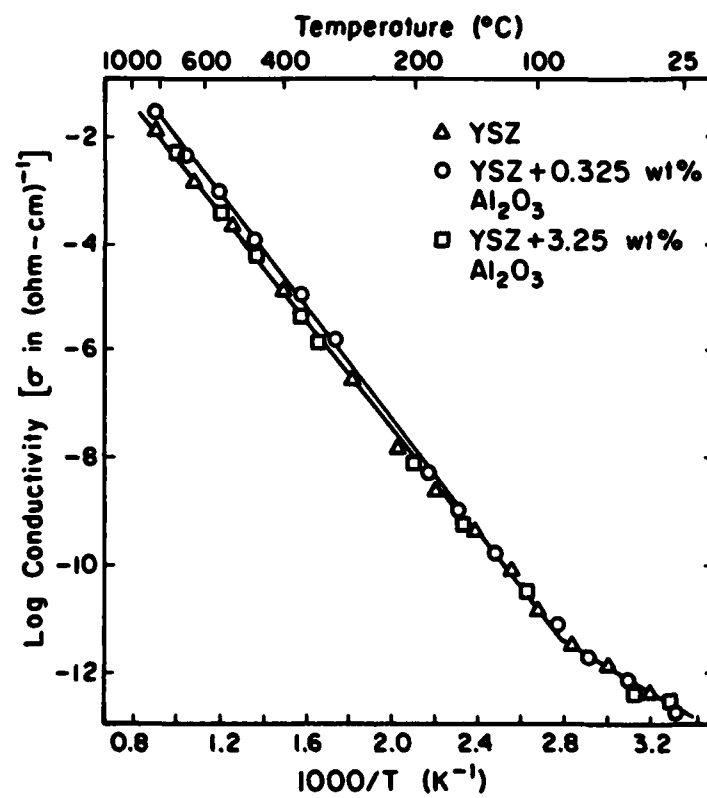


Figure 13. DC conductivity of YSZ-Al<sub>2</sub>O<sub>3</sub> samples as a function of reciprocal temperature

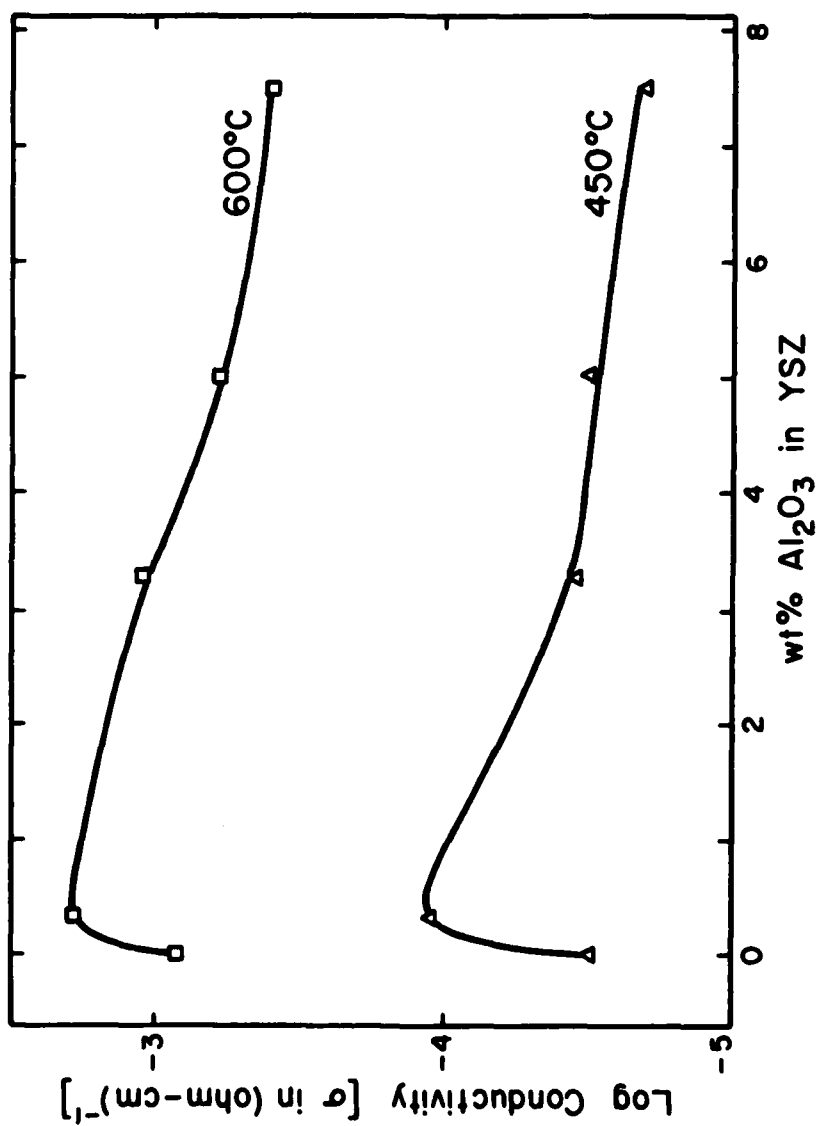


Figure 14. Variation of dc conductivity with added Al<sub>2</sub>O<sub>3</sub> to YSZ at 600°C and 450°C for 0-7.5 wt% Al<sub>2</sub>O<sub>3</sub>.

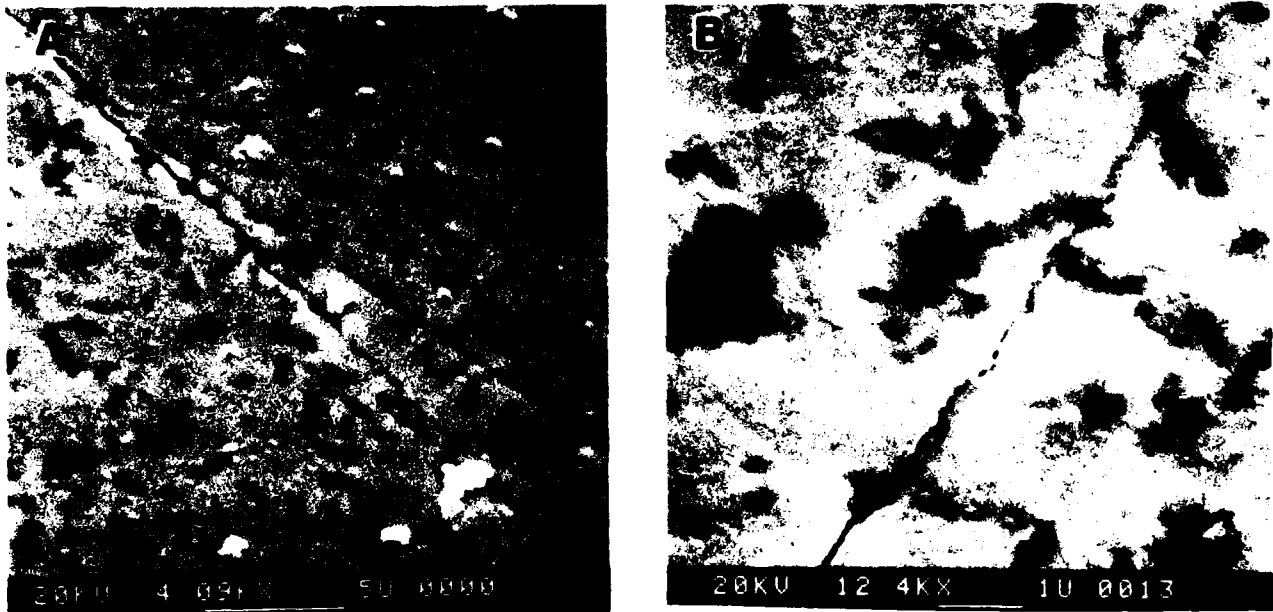


Figure 15. SEM photomicrographs of YSZ + 5.0 wt% Al<sub>2</sub>O<sub>3</sub> at (A) 4.09 kX and (B) 12.4 kX magnification showing crack deflection of indentation induced cracking around included Al<sub>2</sub>O<sub>3</sub> grains.

END

FILMED

6-86

DTIC